Research Article | Vol. 29, No. 11 / 24 May 2021 / Optics Express 16639
Optics EXPRESS

Intensity-dependent angular distribution of low-energy electrons generated by intense high-frequency laser pulse

JINTAI LIANG,[1] WEICHAO JIANG,[2] YIJIE LIAO,[1] QINGHUA KE,[1] MIAO YU,[1] MIN LI,[1] YUEMING ZHOU,[1,4] AND PEIXIANG LU[1,3,5]

[1] *Wuhan National Laboratory for Optoelectronics and School of Physics, Huazhong University of Science and Technology, Wuhan 430074, China*
[2] *College of Physics and Optoelectronic Engineering, Shenzhen University, Shenzhen 518060, China*
[3] *Hubei Key Laboratory of Optical Information and Pattern Recognition, Wuhan Institute of Technology, Wuhan 430205, China*
[4] *zhouymhust@hust.edu.cn*
[5] *lupeixiang@hust.edu.cn*

Abstract: By solving the three-dimensional time-dependent Schrödinger equation, we investigate the angular distributions of the low-energy electrons when an intense high-frequency laser pulse is applied to the hydrogen atom. Our numerical results show that the angular distributions of the low-energy electrons which generated by the nonadiabatic transitions sensitively depend on the laser intensity. The angular distributions evolve from a two-lobe to a four-lobe structure as the laser intensity increases. By analyzing nonadiabatic process in the Kramers-Henneberger frame, we illustrate that this phenomenon is attributed to the intensity-dependent adiabatic evolution of the ground state wavefunction. When the laser intensity further increases, the pathway of nonadiabatic transition from the ground state to the excited state and then to the continuum states is non-negligible, which results in the ring-like structure in the photoelectron momentum distribution. The angular distributions of the low-energy electrons provide a way to monitor the evolution of the electron wavefunction in the intense high frequency laser fields.

1. Introduction

The development of the free-electron laser technology, which is capable of generating extreme ultraviolet (XUV) lasers pulses with unprecedented intensity [1–6], has attracted quite a lot of attentions on the laser-matter interaction in high-frequency regime. Many remarkable and counterintuitive phenomena in high-frequency regime have been actively studied in recent years. One of them is the atomic stabilization, which has been understood as the formation of metastable Kramers-Henneberger (KH) states of the dressed potential [7–12]. Experimentally, this phenomenon has been observed in Rydberg states [13–15].

Numerous investigations on the atomic stabilization in high-frequency regime focus on monochromatic laser pulse, and the high-frequency Floquet theory (HFFT) has been employed to explore the underlying dynamics. However, for real laser pulse, the pulse duration is finite and there are the rising and falling edges, which could induce many interesting effects not accounted for by the HFFT. An adiabatic version of the HFFT taking account of the pulse envelope has been proposed [16,17]. This approach has been successful in understanding the pulse envelope variation induced phenomena, such as the dynamic interference, which originates from the interference of the electron wave packets ejected on the rising and falling edges of the laser pulse [17–25].

Another interesting issue due to the finite pulse duration is the ionization by nonadiabatic transition. As one of the most basic mechanisms of the universe, nonadiabatic transition occurs

#423545 https://doi.org/10.1364/OE.423545
Journal © 2021 Received 24 Feb 2021; revised 28 Apr 2021; accepted 28 Apr 2021; published 14 May 2021

Optics EXPRESS

when the adiabatic parameter changes quickly [26,27]. One of the most well-known examples of the nonadiabatic transition is the transition between the adiabatic electronic states defined by the Born-Oppenheimer approximation when the nuclear motion is involved [28,29]. In the intense high-frequency laser pulses with short duration, the rapid turn-on and turn-off of the laser pulse could induce nonadiabatic transition. It has been shown that the turn-on of the short pulse could induce nonadiabatic transition from the ground state to the excited states, which has been revealed by tracing the time-dependent electrons wave packet of the bound state in the intense high-frequency pulses [7,30–34]. The nonadiabatic transition also occurs from ground state to continue states, resulting in low-energy electrons generation in the intense high-frequency laser pulse [35–38]. These low-energy photoelectrons have attracted considerable attention in the past decades. For example, the modulation in the energy spectrum of the low-energy electrons, which originates from interference of the electrons generated by nonadiabatic transition on the rising and falling edges of the laser pulse, has been detaildedly surveyed [39]. The similar nonadiabatic ionization of Rydberge states has been theoretically and experimentally observed [40,41]. The investigations on the nonadiabatic transition deepen the understanding of the electrons dynamics in the high-frequency regime. In most of previous investigations on the nonadiabatic ionization, attentions mainly focus on the energy spectrum of the electrons [37–39]. With the development of the experimental technique, it is feasible to detect the photoelectron momentum distributions (PEMDs) induced by the high-frequency laser pulse. The PEMDs can provide more information about the electrons dynamics in the nonadiabatic transitions.

In this work, we investigate the angular distributions of the low-energy electrons generated due to nonadiabatic ionization in the intense high-frequency laser pulse. The PEMDs obtained by numerically solving the three-dimensional (3D) time-dependent Schrödinger equation (TDSE) show that the low-energy photoelectron angular distributions (LEPADs) sensitively depend on the laser intensity. It changes from a two-lobe structure to a four-lobe structure as the laser intensity increases. By analyzing the nonadiabatic transitions in the KH frame, we show that the change of the LEPAD originates from intensity dependent evolution of the ground-state wavefunction. As the laser intensity further increases, a ring-like structure appears in momentum distribution of the low-energy electrons, which is attributed to the nonadiabatic transition from the ground state to an excited state followed by the nonadiabatical ionization. The momentum distributions of the low-energy electrons are the manifestation of the adiabatic evolution wavefunction, and thus it provides us a way to monitor the evolution of the electron wavefunction.

This paper is organized as follows. In Sec. 2., we introduce our method for numerically solving the 3D TDSE and the method of treating the nonadiabatic transition. Then we show our numerical results and discussions in Sec. 3. Section. 4. provides a brief summary.

2. Theoretical methods

2.1. Numerically solving TDSE

We obtain the PEMDs by numerically solving the 3D TDSE. The TDSE in velocity gauge is written as (atomic units are used unless otherwise stated):

$$i\frac{\partial\Psi(\mathbf{r},t)}{\partial t} = \left(\frac{1}{2}\mathbf{p}^2 + \mathbf{A}(t)\cdot\mathbf{p} + V(\mathbf{r})\right)\Psi(\mathbf{r},t), \tag{1}$$

where $V(\mathbf{r}) = -1/r$ is Coulomb potential of H. The laser field is described as

$$\mathbf{A}(t) = A_0 f(t)\cos(\omega t)\mathbf{e_z}, \tag{2}$$

where A_0 and ω are the amplitude of the vector potential and center frequency of the laser pulse, respectively. $f(t)$ is the envelope of the laser pulses. In our calculations, we consider two types of

Optics EXPRESS

pulses, the Gaussian shape laser pulse,

$$f(t) = \exp[-2\ln 2(t/\Delta)^2], \tag{3}$$

and the $\sin^2$ shape laser pulse,

$$f(t) = \sin^2(\pi t/\tau + \frac{\pi}{2}). \tag{4}$$

Here, Δ and τ are the full width at half maximum (FWHM) for the Gaussian shape laser pulse and the pulse duration for the $\sin^2$ shape laser pulse, respectively.

In our simulation, the TDSE in Eq. (1) is solved in the spherical coordinates, in which the wave function $\Psi(\mathbf{r}, t)$ is expanded by spherical harmonics $|l, m\rangle$,

$$|\Psi(\mathbf{r}, t)\rangle = \sum_{l,m} \frac{R_{l,m}(r, t)}{r} |l, m\rangle, \tag{5}$$

where $R_{l,m}(r, t)$ is the radial part of the wave function. This radial wave function is discretized by the finite-element discrete variable representation (FE-DVR) method [42]. The angular momentum number l is chosen up to 30, and the convergence has been ensured by varying the number of included partial waves. The time propagation of the TDSE is calculated by the split-Lanczos method [43] with the time step fixed at $\Delta t = 0.01$ a.u.. The maximal box size for the radial coordinates is chosen to be 400 a.u.. An absorbing mask function has been applied in each step of time propagation of the wavefunction, which is written as $F(r) = 1 - 1/(1 + e^{(r-R_c)/L})$ with $R_c = 300$ a.u. and $L = 2$ a.u.. The wavefunction $\Psi(\mathbf{r}, \mathbf{t})$ is split into the inner part $\Psi_{\text{in}}(\mathbf{r}, t) = \Psi(\mathbf{r}, t)F(r)$ and the outer part $\Psi_{\text{out}} = \Psi(\mathbf{r}, t) - \Psi_{\text{in}}(\mathbf{r}, t)$ by the absorbing mask function. The inner wave function is still evolved strictly as TDSE, while the outer part Ψ_{out} is propagated by Coulomb-Volkov propagator [44]. The initial wavefunction is prepared by imaginary-time propagation which is chosen as the ground state of H atom. The ionization amplitude is extracted from the final wavefunction by projecting it to the scattering state [43],

$$M(\boldsymbol{p}) = \langle \Psi_{\boldsymbol{p}}(\mathbf{r}) | \Psi(\mathbf{r}, t_f) \rangle. \tag{6}$$

Here, $\Psi_{\boldsymbol{p}}(\mathbf{r})$ is the normalized scattering state for H atom, which is normalized by $\int d\mathbf{r} \Psi^*_{\boldsymbol{p}}(\mathbf{r}) \Psi_{\boldsymbol{p'}}(\mathbf{r}) = 2\pi\delta(\boldsymbol{p} - \boldsymbol{p'})$. Note that the nondipole effect is not considered here, because the nondipole effect does not affect the angular distributions of the photoelectrons in the polarization plane (the slices of 3D PEMDs at $p_y = 0$) for the laser parameters considered in this work, as discussed in Appendix A..

2.2. Floquet envelope Hamiltonian approach

We adopt the Floquet envelope Hamiltonian approach [16,45–47] to investigate the intensity-dependent LEPAD. By the unitary transformation $\Psi_{\text{KH}}(t) = \exp[i\boldsymbol{\alpha}(t) \cdot \mathbf{p}]\Psi(\mathbf{r}, t)$, the Hamiltonian in Eq. (1) can be transformed to the Hamiltonian in KH frame, which is written as

$$H_{\text{KH}} = \frac{1}{2}\mathbf{p}^2 + V[\mathbf{r} + \boldsymbol{\alpha}(t)], \tag{7}$$

where $\boldsymbol{\alpha}(t) = -\int^t \mathbf{A}(t')dt'$ is the excursion amplitude of the laser pulse. For the linearly monochromatic laser pulse considered in HFFT, the excursion amplitude is written as

$$\boldsymbol{\alpha}(t) = \boldsymbol{\alpha_0} \sin(\omega t), \tag{8}$$

where $\boldsymbol{\alpha}_0 = A_0/\omega \mathbf{e_z}$. The electrons dynamics in the high-frequency regime are described by expanding the laser-distorted Coulomb potential as [48]

$$V(\mathbf{r} + \boldsymbol{\alpha}(t)) = \sum_n V_n(\mathbf{r}; \boldsymbol{\alpha_0}) e^{-in\omega t}. \tag{9}$$

Optics EXPRESS

Here, $V_n(\mathbf{r};\boldsymbol{\alpha_0}) = \int_0^{2\pi} e^{in\chi} V[\mathbf{r}+\boldsymbol{\alpha}(\chi/\omega)]d\chi/(2\pi)$. Then the Hamiltonian can be divided into time-independent H_0 and time-dependent H_I terms

$$H_{\mathrm{KH}} = \underbrace{\frac{1}{2}\mathbf{p}^2 + V_0(\mathbf{r};\boldsymbol{\alpha_0})}_{H_0} + \underbrace{\sum_{n\neq 0} V_n(\mathbf{r};\boldsymbol{\alpha_0})e^{-in\omega t}}_{H_I}. \tag{10}$$

In the lowest-order of the HFFT, the electron is in a stationary state of H_0. The interaction determined by H_I represents multiphoton decay channels, which is taken into account in the higher order of the HFFT.

For the short intense laser pulse considered in this work, effect of the pulse envelope is non-negligible and correction is implemented by the substitution [17]

$$\boldsymbol{\alpha}_0 = \frac{A_0}{\omega}\mathbf{e_z} \rightarrow \boldsymbol{\alpha_0} = \alpha_0(t)\mathbf{e_z} = \frac{A_0}{\omega}f(t)\mathbf{e_z}, \tag{11}$$

where $f(t)$ is envelope of the laser pulse. It indicates that the laser distorted potential $V_0(\mathbf{r};\boldsymbol{\alpha_0})$ is time-depend and follows the envelope of the laser pulse. Then the instantaneous eigenvalue $E_n(\alpha_0)$ and eigenstate $|\phi_n(\alpha_0)\rangle$ of H_0 are determined by

$$\left(\frac{1}{2}\mathbf{p}^2 + V_0(\mathbf{r};\boldsymbol{\alpha_0})\right)|\phi_n(\alpha_0)\rangle = E_n(\alpha_0)|\phi_n(\alpha_0)\rangle. \tag{12}$$

The time-dependent electron wave packet $|\Psi_{\mathrm{KH}}(t)\rangle$ can be expanded by the instantaneous eigenstates of H_0,

$$|\Psi_{\mathrm{KH}}(t)\rangle = \sum\!\!\!\!\!\!\int_n C_n(t)e^{-i\int^t d\tau E_n(\tau)}|\phi_n(\alpha_0)\rangle. \tag{13}$$

Inserting the wavefunction $|\Psi(t)\rangle$ into the Schrödinger equation with the Hamiltonian H_{KH} in Eq. (10), the evolution of time-dependent amplitudes $C_n(t)$ is determined by

$$\dot{C}_n(t) = \sum\!\!\!\!\!\!\int_m \langle\phi_n|\left(-\frac{\partial\alpha_0}{\partial t}\frac{\partial}{\partial\alpha_0} - iH_I\right)|\phi_m\rangle e^{-i\int^t d\tau(E_m-E_n)}C_m(t). \tag{14}$$

The term $\langle\phi_n|H_I|\phi_m\rangle$ represents the photon absorption or emission, and the term $\langle\phi_n|\frac{\partial}{\partial\alpha_0}|\phi_m\rangle$ provides nonadiabatic coupling. In this work, we focus on the nonadiabatic transition originating from the derivatives of the laser pulse envelope and dynamics of the low-energy electrons generated by the nonadiabatic transition, which is independent on the term $\langle\phi_n|H_I|\phi_m\rangle$ [37,45]. Thus the term $\langle\phi_n|H_I|\phi_m\rangle$ is not considered in the rest of discussions. Then the time-dependent amplitudes of the bound and the continuum states in the nonadiabatic transitions can be written as

$$C_n(t) = -\sum\!\!\!\!\!\!\int_m \int^t d\tau\langle\phi_n|\frac{\partial}{\partial\alpha_0}|\phi_m\rangle\frac{\partial\alpha_0}{\partial\tau}e^{-i\int^\tau d\tau'(E_m-E_n)}C_m(\tau), \tag{15}$$

and

$$C_{\boldsymbol{p}}(t) = -\sum\!\!\!\!\!\!\int_m \int^t d\tau\langle\phi_{\boldsymbol{p}}|\frac{\partial}{\partial\alpha_0}|\phi_m\rangle\frac{\partial\alpha_0}{\partial\tau}e^{-i\int^\tau d\tau'(E_m-E_k)}C_m(\tau). \tag{16}$$

Here, $\phi_{\boldsymbol{p}}$ is approximately chosen as the normalized scattering state for H atom and $\frac{\partial}{\partial\alpha_0}|\phi_m\rangle$ is derivative of the wavefunction. Eq. (16) indicates that if the eigenenergies and eigenstates of H_0 are acquired by solving Eq. (12), the PEMDs of the low-energy electrons generated by the nonadiabatic transition can be obtained. In addition, this approach also helps us identify the contributions of the different nonadiabatic transition channels.

Optics EXPRESS

3. Results and discussions

Figure 1 shows the PEMDs for the ionization of H obtained by solving the 3D TDSE. The parameters for the Gaussian shape laser pulses are $\omega = 3$ a.u. and $\Delta = 5T$. The laser intensities for Figs. 1(a)–1(d) are 1×10^{14} W/cm^2, 4×10^{18} W/cm^2, 8×10^{18} W/cm^2 and 2×10^{19} W/cm^2, respectively. For the lowest intensity [Fig. 1(a)], the PEMD reveals a ring-like structure and the radius of the ring is $p = \sqrt{2(\omega - I_p)}$. This is characteristic of the single-photon ionization from ground state of H atom. As the intensity increases to 4×10^{18} W/cm^2 [Fig. 1(b)], two ring-like structures appear in the high energy region, which originate from the single- and two-photon ionization. The modulations on the ring-like structures originate from the dynamic interference [17–20]. Surprisingly, low-energy photoelectrons appear in the PEMD. Because the photon energy is much higher than the ionization potential of the atom, these electrons can not be attributed to the photon absorption process. In previous works, the low-energy electrons have been observed in the investigations on the ionization of H^- [37,39] and clusters [38]. It is demonstrated that the low-energy electrons are generated via the nonadiabatic transitions due to the finite length of the laser pulse. This can be verified by calculating the ionization of the atom for the longer laser pulse, as shown in Fig. 2. With the increasing of the duration of the laser pulse, the yield of the low-energy photoelectrons decreases [Fig. 2(a)]. When the pulse duration further increases to Δ=20T, as shown in Fig. 2(b), the low-energy photoelectrons disappear. To further verify that the low-energy electrons are generated by the nonadiabatic transitions, we change the envelope of the laser pulse. For the sin^2 shape laser pulse, as shown in Figs. 2(c) and 2(d), the low-energy photoelectrons appear in the PEMD for τ=30T and disappear for a longer laser pulse. More interestingly, our results show that the angular distributions of the low-energy electrons sensitively depend on the laser intensity as displayed in Fig. 1. For example, the LEPAD exhibits a two-lobe structure for $I_0 = 4 \times 10^{18}$ W/cm^2 [Fig. 1(b)], and a four-lobe structure for more intense laser pulse [Fig. 1(c)]. When the laser intensity further increases, as shown in Fig. 1(d), a ring-like structure appears in the PEMD. As far as we know, the intensity-dependent LEPAD has not been observed and investigated previously. In the following, we will focus on the intensity-dependent LEPADs and choose the Gaussian shape laser pulse used in Fig. 1 as an example.

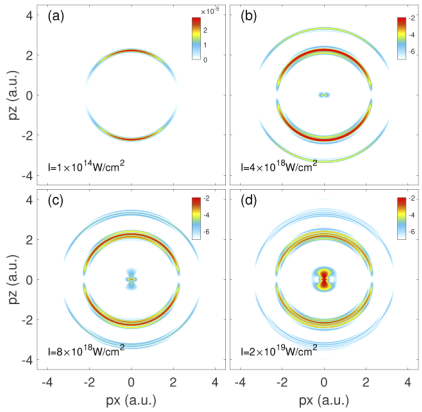

Fig. 1. PEMDs for the ionization of H atom by numerically solving the TDSE. The laser intensities for (a)-(d) are $I_0 = 1 \times 10^{14}$ W/cm^2, $I_0 = 4 \times 10^{18}$ W/cm^2, $I_0 = 8 \times 10^{18}$ W/cm^2 and $I_0 = 2 \times 10^{19}$ W/cm^2, respectively. The parameters for the Gaussian shape laser pulses are $\omega = 3$ a.u. and $\Delta = 5T$. Note that (b)-(d) are the PEMDs in logarithmic scale.

We adopt the Floquet envelope Hamiltonian approach as shown in Sec. 2.2 to understand the intensity-dependent LEPADs. In this approach, the evolution of the wavefunction is described on

Optics EXPRESS

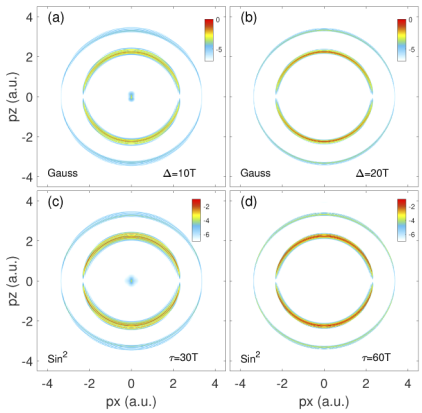

Fig. 2. PEMDs for the ionization of H atom by numerically solving the TDSE for different envelopes of the laser pulse (a) Gaussian shape, $\Delta = 10T$, (b) Gaussian shape, $\Delta = 20T$, (c) $\sin^2$, τ=30T, (d) $\sin^2$, τ=60T. The other laser parameters are the same as those in Fig. 1(d).

the basis of the eigenstates of the Hamiltonian H_0 in Eq. (10). The eigenvalue problem, Eq. (12), is solved by diagonalization of the Hamiltonian matrix in Lagrange interpolating polynomials basis [42] and the eigenenergies for three lowest-lying bound states are shown in Fig. 3(a). As indicated by Eq. (16), the nonadiabatic transition rates of the continuum states depend on the term $\partial\alpha_0/\partial\tau$. It implies that the nonadiabatic transition depends on the derivatives of the laser pulse envelope rather than the envelope itself. For the Gaussian shape laser pulse, the derivative of excursion amplitude reveals a double-peak structure and the peaks locate at -t_s and t_s, as shown in Fig. 3(b). The contributions of transitions at these two instants are the same and dominate in the entire pulse duration. Thus, we only consider the nonadiabatic transition at one of these two peaks, i.e., the transition at t_s. Since the laser pulse is short and the laser intensity is low enough, the interference effect caused by the phase accumulated as the time propagation, $\exp[-i\int^{\tau} d\tau'(E_m - E_k)]$, is ignored. The term $C_m(\tau)$ describes the depletion of the states. We choose the ground state of H as the initial state, and the depletion of $1s\sigma_g$ state is neglected in the zero-order approximation. Therefore, the momentum distributions of electrons ionized by the nonadiabatic transitions from the ground state can be approximately written as

$$M_{NA}(\boldsymbol{p}) \sim \langle\phi_{\boldsymbol{p}}|\frac{\partial}{\partial\alpha_0(t_s)}|1s\sigma_g\rangle\frac{\partial\alpha_0}{\partial\tau}\Big|_{\tau=t_s}. \tag{17}$$

It implies that the angular distributions of the low-energy electrons are mainly determined by the derivatives of wavefunction at transition moment t_s. For the Gaussian shape laser pulse, the transition moment is given by $t_s = \Delta/2\sqrt{\ln 2}$. Then $\alpha_0(t_s) = e^{-1/2}\sqrt{I_0}/\omega^2$, which monotonously increases with the laser intensity. It indicates that the derivative of wavefunction at transition moment t_s depends on the laser intensity. Therefore, the LEPAD sensitively depends on the laser intensity.

To verify the validity of Eq. (17) in describing the LEPADs, we compare the TDSE data with the results obtained by Eq. (17) in Fig. 4. The dot dashed lines represent the LEPADs, which are obtained by the integration of the PEMDs from p=0 a.u. to p=0.5 a.u. The results show that the amplitude of the angular distribution along the polarization direction increases as the increasing of laser intensity, and then the momentum distributions change from a two-lobe structure to a four-lobe structure. Apparently, the results calculated by Eq. (17) agree well with the TDSE data. It indicates that Eq. (17) is valid to describe the LEPADs, and the low-energy electrons are generated mainly by the nonadiabatic transition from the ground state in these laser intensities.

Optics EXPRESS

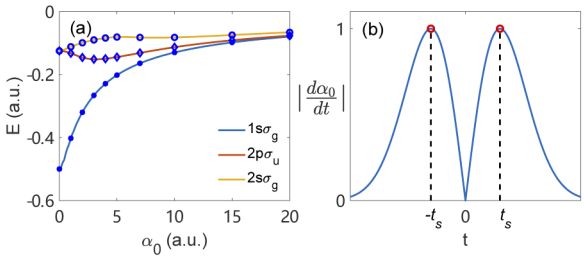

Fig. 3. (a) The eigenenergies of Hamiltonian H_0 in Eq. (10) as a function of α_0 for $1s\sigma_g$ (blue line), $2p\sigma_u$ (red line), and $2s\sigma_g$ (yellow line) state. The symbols are the results from previous work [49]. (b) The absolute value of derivative of the time-dependent excursion amplitude of the laser pulse in Eq. (11). t_s and $-t_s$ are the instants of the peaks of the derivative of α_0 which are marked by the red circles.

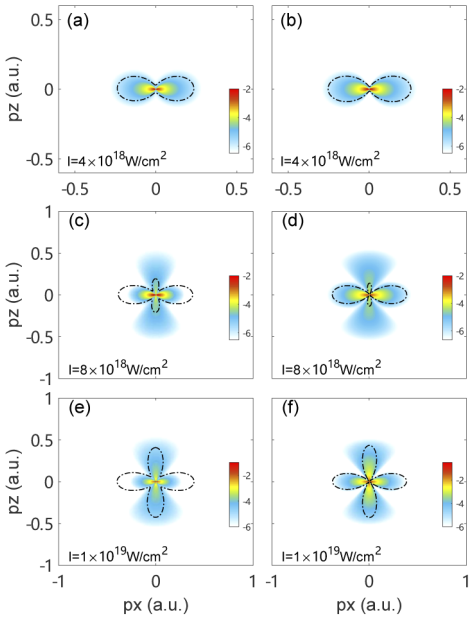

Fig. 4. Comparison between the TDSE data (left panels) and the results obtained by Eq. (17) (right panels). The laser intensities for the top, middle and bottom panels are $I_0 = 4 \times 10^{18}$ W/cm^2, $I_0 = 8 \times 10^{18}$ W/cm^2, $I_0 = 1 \times 10^{19}$ W/cm^2, respectively. The dot dashed lines represent the LEPAD for the corresponding PEMDs. Note that the PEMDs are shown in logarithmic scale.

Optics EXPRESS

Actually, the nonadiabatic transition occurs not only from the ground state to the continuum state but also to the excited states. Figure 5 shows time-dependent populations of the excited states for the nonadiabatic transition from the ground state $1s\sigma_g$ obtained by Eq. (15). Since the operator $\partial/\partial\alpha_0$ does not change parity of the states, the nonadiabatic transition only exists between the states with the same parity. Therefore, the population of $2p\sigma_u$ state is zero for both laser intensities, as shown by the blue lines. For $2s\sigma_g$ state, as shown by the red dashed line, the population of this state is less than three percent for $I_0 = 4 \times 10^{18}$ W/cm^2. When the laser intensity increases to 2×10^{19} W/cm^2, the population of $2s\sigma_g$ state is nearly twenty percent. Therefore, the nonadiabatic ionization from $2s\sigma_g$ state should be considered.

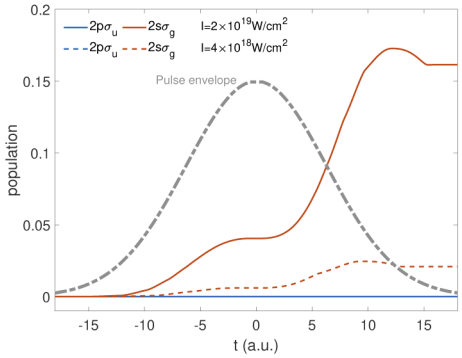

Fig. 5. The time-dependent population of the excited states for the laser intensity of $I_0 = 2 \times 10^{19}$ W/cm^2 (solid lines) and $I_0 = 4 \times 10^{18}$ W/cm^2 (dashed lines) obtained by Eq. (15). The blue and red lines are the results for $2p\sigma_u$ and $2s\sigma_g$ state, respectively. The gray dot dashed line represents the envelope of the laser pulse.

In Fig. 6(a), we show the PEMD obtained by solving the TDSE with the laser intensity of $I_0 = 2 \times 10^{19}$ W/cm^2. As indicated by the dot dashed lines, the angular distributions in the lower (black line) and higher (red line) energy region reveal different structures, i.e., a four-lobe structure for the lower energy region and a ring-like structure for the higher energy region. The difference of the angular distributions implies that there are two different nonadiabatic transition channels for the low-energy electrons. We calculate the PEMDs for the nonadiabatic ionization from $1s\sigma_g$ state and $2s\sigma_g$ state by Eq. (16), as shown in Figs. 6(b) and 6(c). The dot dashed lines represent the angular distributions for corresponding PEMDs. It indicates that the nonadiabatic transition from $1s\sigma_g$ state exhibits four-lobe structure and the transition from $2s\sigma_g$ state reveals ring-like structure. The difference of the angular distributions reflects the different wavefunction derivatives at the nonadiabatic transition moment t_s of these two states. As shown by the insets of Figs. 6(b) and 6(c), the derivative of wavefunction with respect to α_0 exhibits a three-lobe structure for $1s\sigma_g$ state and a ring-like structure for $2s\sigma_g$ state.

As discussed above, the LEPADs are mainly determined by the wavefunction derivative at the transition instant t_s. To further understand the dependence of the angular distributions on the derivative of wavefunction with respect to α_0, we calculate the weights of the partial waves of the wavefunction and the wavefunction derivative of the $1s\sigma_g$ state by

$$W_l^W(\alpha_0) = \int_0^\infty r^2 \left|\langle l, 0|\Psi_{1s\sigma_g}(\alpha_0)\rangle\right|^2 dr, \tag{18}$$

and

$$W_l^{DW}(\alpha_0) = \int_0^\infty r^2 \left|\langle l, 0|\frac{\partial}{\partial\alpha_0}|\Psi_{1s\sigma_g}(\alpha_0)\rangle\right|^2 dr. \tag{19}$$

Optics EXPRESS

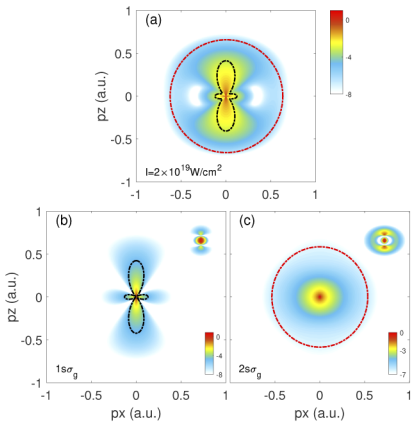

Fig. 6. (a) PEMD for the ionization of H atom by numerically solving the TDSE with the laser intensity $I_0 = 2\times10^{19}$ W/cm^2. The black and red dot dashed lines represent the angular distributions for the lower ($0<|\boldsymbol{p}|<0.5$) and higher ($0.8<|\boldsymbol{p}|<1$) energy region, respectively. (b) The PEMD for the nonadiabatic transition from $1s\sigma_g$ state obtained by Eq. (16). The dot dashed line represents the angular distribution of the PEMD. The inset shows the derivatives of the wavefunction at the nonadiabatic transition t_s. (c) Same as (b) but for $2s\sigma_g$ state.

Here, $|l, m\rangle$ is the spherical harmonics. Since the laser pulse is linearly polarized along the z axis, the magnetic quantum number m is conserved. As a consequence, we only need to consider the component of m=0. As shown in Fig. 7(a), for the wavefunction, the weights of the partial waves are roughly unchanged as α_0 increases. While for the wavefunction derivatives with respect to α_0, the weight of l=0 decreases and the weight of l=2 increases as the increasing of α_0. The l=0 partial wave produces a isotropy structure and the l=2 partial wave exhibits a four-lobe structure in the momentum space. The PEMDs for the low-energy electrons can be thought as the superposition of these two components. Therefore, as shown in Fig. 7(b), the momentum distributions of the low-energy electrons change from a isotropy structure to a four-lobe structure as α_0 increases. To quantitatively identify the contributions of the s (l=0) and d (l=2) wave to the LEPADs, we use the following formula to describe the LEPADs

$$P(\theta) = C[1 + \beta_2 P_2(\cos\theta) + \beta_4 P_4(\cos\theta)]. \tag{20}$$

Here, C is the normalization constant, $\beta_{2,4}$ are the second- and fourth-order anisotropy parameters, and $P_{2,4}$ are the second- and fourth-order Legendre polynomials [50]. $\beta_{2,4}$ are obtained by projecting the angular distributions of low-energy electrons (Integration of the PEMD from 0 a.u. to 0.5 a.u.) to the corresponding Legendre polynomials. The ratio β_2/β_4 as a function of laser intensity is shown in Fig. 7(c), in which the circle solid line and the triangle dashed line are for the TDSE data and the results obtained by Eq. (17), respectively. Apparently, the agreement between these results is remarkable, which further verifies the validity of Eq. (17) to describe the angular distribution of the low-energy electrons. Moreover, the increasing of the ratio as laser intensity represents that the contributions of d wave increases as the laser intensity and then the LEPAD evolves from the two-lobe structure to the four-lobe structure.

The PEMD is a manifestation of the wavefunction derivative, as indicated by Eq. (17). Thus, it provides us a way to trace the evolution of the wavefunction derivative. For the Gaussian pulses, the low-energy photoelectrons are mainly released at two instants, $-t_s$ and t_s. For the short pulses in our calculations, the interference between electrons released at these two instants is negligible. Then we reconstruct the wavefunction derivative according to Eq. (17). Note that there is no phase information in the PEMDs and thus in our reconstruction we do not consider the

Optics EXPRESS

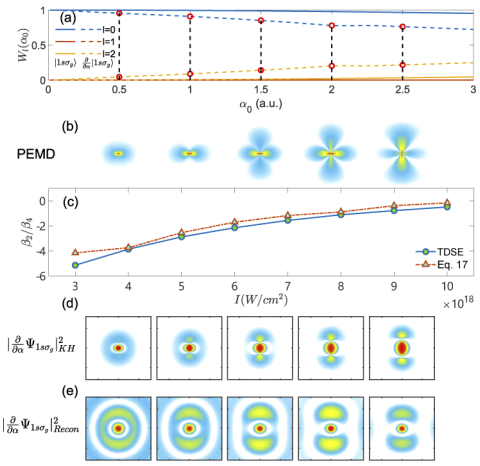

Fig. 7. (a) The weights of the partial waves for the wavefunction $|1s\sigma_g\rangle$ (solid lines) and the derivative of the wavefunction $\frac{\partial}{\partial\alpha_0}|1s\sigma_g\rangle$ (dashed lines) as a function of α_0. The blue, red and yellow lines are the results for $l = 0, 1, 2$, respectively. (b) The LEPADs related to the derivatives of the wavefunction at selected α_0 marked with red circles in (a). (c) The ratio of the asymmetry parameter β_2/β_4 as a function of the laser intensity. The circle solid line and the triangle dashed line are for the TDSE data and the results obtained by Eq. (17), respectively. (d) The derivatives of the ground state wavefunction with respect to α_0 for H_0 in Eq. (10) corresponding to the PEMDs in (b). (e) Same as (d) but for the reconstruction results.

phase of the factor $\langle\phi_{\boldsymbol{p}}|\frac{\partial}{\partial\alpha_0(t_s)}|1s\sigma_g\rangle$. The results are shown in Fig. 7(e). The exact wavefunction derivatives with respect to α_0 are also shown for comparison in Fig. 7(d). The reconstructed results agree reasonably well with the exact results. The additional structures appearing in the large coordinate range might be due to the limited bandwidth of the electron spectrum. The similar problem also exists in the tomographic imaging of molecular orbitals [51].

4. Conclusion

In conclusion, we have investigated the angular distributions of the low-energy electrons generated by nonadiabatic transition. By numerically solving the 3D TDSE, we find that the LEPAD sensitively depends on the laser intensity. It changes from a two-lobe structure to a four-lobe structure as the laser intensity increases. By analyzing the nonadiabatic transition in the KH frame, we find that this phenomenon is attributed to the intensity-dependent wavefunction derivatives of the ground state at the transition instant. For the more intense laser pulse, the non-negligible nonadiabatic transition from the excited state results in a ring-like structure in the angular distribution. It indicates that the angular distributions of the low-energy electrons provide a way to directly identify the contributions of different nonadiabatic transition channels. Moreover, utilizing the relationship between the PEMDs of the low-energy electrons with the wavefunction derivative at the transition instant, we successfully monitor the evolution of the ground state wavefunction by the momentum distributions of the low-energy electrons. Our work deepens the understanding of the nonadiabatic transitions in the intense high-frequency laser pulse.

A. Nondipole effect of the low-energy electrons

For the intense laser field, the nondipole effect is important. In previous works [36,52,53], the nondipole effect for the low-energy electrons are investigated. To test the validity of the

Optics EXPRESS

dipole approximation in analyzing the generation of the low-energy electrons, the lowest-order nondipole correction is considered. The lowest-order nondipole corrected Hamiltonian in the velocity gauge is written as

$$H_{\mathrm{ND}} = -\frac{1}{2}\nabla^2 + V(r) - i\mathbf{A}(t)\cdot\nabla + \frac{1}{c}(\mathbf{k}\cdot\mathbf{r})[\mathbf{A}(t)\cdot\mathbf{F}(t)] - i\frac{1}{c}(\mathbf{k}\cdot\mathbf{r})\mathbf{F}(t)\cdot\nabla. \tag{A1}$$

Here, $\mathbf{A}(t)$ and $\mathbf{F}(t)$ are the usually adopted vector potential and electric field of the laser pulse in the dipole approximation, respectively. In our simulation, the laser pulse propagates along the positive y-axis and is polarized along the z-axis.

We numerically solved the 3D TDSE within nondipole correction in spherical coordinates and the details have been shown in our previous work [20]. Figure 8 shows the PEMDs for the ionization of H atom with the highest laser intensity considered in our work; i.e., $I_0 = 2\times10^{19}$ W/cm^2. The upper and bottom panels are the results with dipole approximation and the lowest nondipole correction, respectively. Obviously, the nondipole effect results in the asymmetry distribution in the plane with the laser propagation direction as shown in Figs. 8(b) and 8(d). The similar asymmetry is also displayed in previous works [36,52,53]. However, the nondipole effect does not affect the angular distribution of low-energy electrons in the polarization plane (p_x-p_z) for the laser parameters considered here, as shown in Figs. 8(a) and 8(c). As indicated by previous work [52], when the amplitude of electric field is larger than 30 a.u., the dipole approximation begins to break down due to strong influence of the generation of the low-energy electrons by nondipole correction and then the PEMD in polarization plane is different from the results with dipole approximation. However, the amplitude of electric field for the highest laser intensity considered in this work ($I_0 = 2\times10^{19}$ W/cm^2, E_0=23.8 a.u.) is less than 30 a.u.. Therefore, it is valid to analysis the PEMD in polarization plane with dipole approximation for the laser parameter considered in our work.

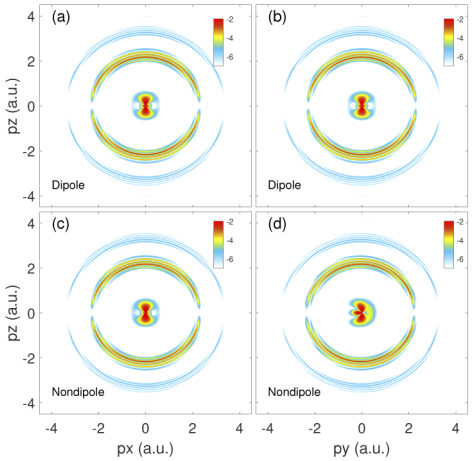

Fig. 8. PEMDs for the ionization of H atom by numerically solving the TDSE within dipole approximation (a) and (b) and nondipole correction (c) and (d) for a $\hat{z}$-polarized pulse propagating in the positive $\hat{y}$ direction. The laser intensity is 2×10^{19} W/cm^2 and the other laser parameters are the same as Fig. 1. The left and right panels are the PEMDs in the p_x-p_z and p_y-p_z plane.

Funding. National Key Research and Development Program of China (2019YFA0308300); National Natural Science Foundation of China (11804233, 11874163, 12021004, 12074265).

Optics EXPRESS

Acknowledgments. Numerical simulations presented in this paper were carried out using the High Performance Computing Center experimental testbed in SCTS/CGCL.

Disclosures. The authors declare no conflicts of interest.

References

1. M. W. Guetg, A. A. Lutman, Y. Ding, T. J. Maxwell, F. J. Decker, U. Bergmann, and Z. Huang, "Generation of highpower high-intensity short x-ray free-electron-laser pulses," Phys. Rev. Lett. **120**(1), 014801 (2018).
2. T. Ishikawa, H. Aoyagi, T. Asaka, Y. Asano, N. Azumi, T. Bizen, H. Ego, K. Fukami, T. Fukui, Y. Furukawa, S. Goto, H. Hanaki, T. Hara, T. Hasegawa, T. Hatsui, A. Higashiya, T. Hirono, N. Hosoda, M. Ishii, T. Inagaki, Y. Inubushi, T. Itoga, Y. Joti, M. Kago, T. Kameshima, H. Kimura, Y. Kirihara, A. Kiyomichi, T. Kobayashi, C. Kondo, T. Kudo, H. Maesaka, X. M. Marechal, T. Masuda, S. Matsubara, T. Matsumoto, T. Matsushita, S. Matsui, M. Nagasono, N. Nariyama, H. Ohashi, T. Ohata, T. Ohshima, S. Ono, Y. Otake, C. Saji, T. Sakurai, T. Sato, K. Sawada, T. Seike, K. Shirasawa, T. Sugimoto, S. Suzuki, S. Takahashi, H. Takebe, K. Takeshita, K. Tamasaku, H. Tanaka, R. Tanaka, T. Tanaka, T. Togashi, K. Togawa, A. Tokuhisa, H. Tomizawa, K. Tono, S. Wu, M. Yabashi, M. Yamaga, A. Yamashita, K. Yanagida, C. Zhang, T. Shintake, H. Kitamura, and N. Kumagai, "A compact x-ray free-electron laser emitting in the sub-ångström region," Nat. Photonics **6**(8), 540–544 (2012).
3. B. W. J. McNeil and N. R. Thompson, "X-ray free-electron lasers," Nat. Photonics **4**(12), 814–821 (2010).
4. M. Fuchs, M. Trigo, J. Chen, S. Ghimire, S. Shwartz, M. Kozina, M. Jiang, T. Henighan, C. Bray, G. Ndabashimiye, P. H. Bucksbaum, Y. Feng, S. Herrmann, G. A. Carini, J. Pines, P. Hart, C. Kenney, S. Guillet, S. Boutee, G. J. Williams, M. Messerschmidt, M. M. Seibert, S. Moeller, J. B. Hastings, and D. A. Reis, "Anomalous nonlinear x-ray compton scattering," Nat. Phys. **11**(11), 964–970 (2015).
5. R. K. Lam, S. L. Raj, T. A. Pascal, C. D. Pemmaraju, L. Foglia, A. Simoncig, N. Fabris, P. Miotti, C. J. Hull, A. M. Rizzuto, J. W. Smith, R. Mincigrucci, C. Masciovecchio, A. Gessini, E. Allaria, G. De Ninno, B. Diviacco, E. Roussel, S. Spampinati, G. Penco, S. Di Mitri, M. Trovò, M. Danailov, S. T. Christensen, D. Sokaras, T.-C. Weng, M. Coreno, L. Poletto, W. S. Drisdell, D. Prendergast, L. Giannessi, E. Principi, D. Nordlund, R. J. Saykally, and C. P. Schwartz, "Soft x-ray second harmonic generation as an interfacial probe," Phys. Rev. Lett. **120**(2), 023901 (2018).
6. J. Stöhr and A. Scherz, "Creation of x-ray transparency of matter by stimulated elastic forward scattering," Phys. Rev. Lett. **115**(10), 107402 (2015).
7. M. Gavrila, "Atomic stabilization in superintense laser fields," J. Phys. B: At., Mol. Opt. Phys. **35**(18), R147–R193 (2002).
8. A. M. Popov, O. V. Tikhonova, and E. A. Volkova, "Strong field atomic stabilization: numerical simulation and analytical modelling," J. Phys. B: At., Mol. Opt. Phys. **36**(10), R125–R165 (2003).
9. M. Pont, "Atomic distortion and ac-Stark shifts of H under extreme radiation conditions," Phys. Rev. A **40**(10), 5659–5672 (1989).
10. M. Pont and M. Gavrila, "Stabilization of atomic hydrogen in superintense, high-frequency laser fields of circular polarization," Phys. Rev. Lett. **65**(19), 2362–2365 (1990).
11. Q. Su, J. H. Eberly, and J. Javanainen, "Dynamics of atomic ionization suppression and electron localization in an intense high-frequency radiation field," Phys. Rev. Lett. **64**(8), 862–865 (1990).
12. Q. Su and J. H. Eberly, "Suppression of ionization and atomic electron localization by short intense laser pulses," Phys. Rev. A **43**(5), 2474–2479 (1991).
13. M. P. de Boer, J. H. Hoogenraad, R. B. Vrijen, L. D. Noordam, and H. G. Muller, "Indications of high-intensity adiabatic stabilization in neon," Phys. Rev. Lett. **71**(20), 3263–3266 (1993).
14. M. P. de Boer, J. H. Hoogenraad, R. B. Vrijen, R. C. Constantinescu, L. D. Noordam, and H. G. Muller, "Adiabatic stabilization against photoionization: An experimental study," Phys. Rev. A **50**(5), 4085–4098 (1994).
15. N. J. van Druten, R. C. Constantinescu, J. M. Schins, H. Nieuwenhuize, and H. G. Muller, "Adiabatic stabilization: Observation of the surviving population," Phys. Rev. A **55**(1), 622–629 (1997).
16. K. Toyota, O. I. Tolstikhin, T. Morishita, and S. Watanabe, "Siegert-state expansion in the Kramers-Henneberger frame: Interference substructure of above-threshold ionization peaks in the stabilization regime," Phys. Rev. A **76**(4), 043418 (2007).
17. K. Toyota, O. I. Tolstikhin, T. Morishita, and S. Watanabe, "Interference substructure of above-threshold ionization peaks in the stabilization regime," Phys. Rev. A **78**(3), 033432 (2008).
18. M. Baghery, U. Saalmann, and J. M. Rost, "Essential conditions for dynamic interference," Phys. Rev. Lett. **118**(14), 143202 (2017).
19. W.-C. Jiang and J. Burgdörfer, "Dynamic interference as signature of atomic stabilization," Opt. Express **26**(16), 19921 (2018).
20. J. Liang, W.-C. Jiang, S. Wang, M. Li, Y. Zhou, and P. Lu, "Atomic dynamic interference in intense linearly and circularly polarized XUV pulses," J. Phys. B: At., Mol. Opt. Phys. **53**(9), 095601 (2020).
21. P. V. Demekhin and L. S. Cederbaum, "Dynamic interference of photoelectrons produced by high-frequency laser pulses," Phys. Rev. Lett. **108**(25), 253001 (2012).
22. P. V. Demekhin and L. S. Cederbaum, "Coherent intense resonant laser pulses lead to interference in the time domain seen in the spectrum of the emitted particles," Phys. Rev. A **86**(6), 063412 (2012).
23. C. Yu, N. Fu, G. Zhang, and J. Yao, "Dynamic stark effect on XUV-laser-generated photoelectron spectra: Numerical experiment on atomic hydrogen," Phys. Rev. A **87**(4), 043405 (2013).

Optics EXPRESS

24. W.-C. Jiang, S.-G. Chen, L.-Y. Peng, and J. Burgdörfer, "Two- electron interference in strong-field ionization of he by a short intense extreme ultraviolet laser pulse," Phys. Rev. Lett. **124**(4), 043203 (2020).
25. H. Liang, W.-C. Jiang, M.-X. Wang, Q. Gong, K. Krajewska, and L.-Y. Peng, "Dynamical interference of H and H_2^+ in one photon ionization," Phys. Rev. A **101**(5), 053424 (2020).
26. H. Nakamura, *Nonadiabatic Transition* (World Scientific, 2012).
27. T. J. Morgan, C. F. Barnett, J. A. Ray, and A. Russek, "Investigation of nonadiabatic effects in molecular-hydrogen Rydberg states by electric field ionization," Phys. Rev. A **20**(3), 1062–1072 (1979).
28. A. Thiel, "The Landau-Zener effect in nuclear molecules," J. Phys. G: Nucl. Part. Phys. **16**(7), 867–910 (1990).
29. B. Imanishi and W. von Oertzen, "Molecular orbitals of nucleons in nucleus-nucleus collisions," Phys. Rep. **155**(2), 29–136 (1987).
30. K. C. Kulander, K. J. Schafer, and J. L. Krause, "Dynamic stabilization of hydrogen in an intense, high-frequency, pulsed laser field," Phys. Rev. Lett. **66**(20), 2601–2604 (1991).
31. V. C. Reed, P. L. Knight, and K. Burnett, "Supression of ionization in strong laser fields," Phys. Rev. Lett. **67**(11), 1415–1418 (1991).
32. K. Burnett, P. L. Knight, B. R. M. Piraux, and V. C. Reed, "Supression of ionization in strong laser fields," Phys. Rev. Lett. **66**(3), 301–304 (1991).
33. N. J. Kylstra, R. A. Worthington, A. Patel, P. L. Knight, J. R. Vázquez de Aldana, and L. Roso, "Breakdown of stabilization of atoms interacting with intense, high-frequency laser pulses," Phys. Rev. Lett. **85**(9), 1835–1838 (2000).
34. C. J. Joachain, N. J. Kylstra, and R. M. Potvliege, *Atoms in Intense Laser Fields* (Cambridge University, 2011).
35. A. Patel, N. J. Kylstra, and P. L. Knight, "Effect of laser pulse shapes on the stabilization of a model atom," J. Phys. B: At., Mol. Opt. Phys. **32**(24), 5759–5778 (1999).
36. M. Førre, S. Selstø, J. P. Hansen, and L. B. Madsen, "Exact nondipole Kramers-Henneberger Form of the light-atom Hamiltonian: An application to atomic stabilization and photoelectron energy spectra," Phys. Rev. Lett. **95**(4), 043601 (2005).
37. K. Toyota, O. I. Tolstikhin, T. Morishita, and S. Watanabe, "Slow Electrons Generated by Intense High-Frequency Laser Pulses," Phys. Rev. Lett. **103**(15), 153003 (2009).
38. A. C. Garibay, U. Saalmann, and J. M. Rost, "Slow electrons from clusters in strong x-ray pulses," J. Phys. B: At., Mol. Opt. Phys. **48**(17), 174003 (2015).
39. Q.-C. Ning, U. Saalmann, and J. M. Rost, "Electron dynamics driven by light-pulse derivatives," Phys. Rev. Lett. **120**(3), 033203 (2018).
40. R. R. Jones, "Interference effects in the multiphoton ionization of sodium," Phys. Rev. Lett. **74**(7), 1091–1094 (1995).
41. L. Ortmann, C. Hofmann, and A. S. Landsman, "Dependence of Rydberg-state creation by strong-field ionization on laser intensity," Phys. Rev. A **98**(3), 033415 (2018).
42. T. N. Rescigno and C. W. McCurdy, "Numerical grid methods for quantum-mechanical scattering problems," Phys. Rev. A **62**(3), 032706 (2000).
43. W.-C. Jiang and X.-Q. Tian, "Efficient split-lanczos propagator for strong-field ionization of atoms," Opt. Express **25**(22), 26832–26843 (2017).
44. D. G. Arbó, J. E. Miraglia, M. S. Gravielle, K. Schiessl, E. Persson, and J. Burgdörfer, "Coulomb-Volkov approximation for near-threshold ionization by short laser pulses," Phys. Rev. A **77**(1), 013401 (2008).
45. K. Toyota, U. Saalmann, and J. M. Rost, "The envelope hamiltonian for electron interaction with ultrashort pulses," New J. Phys. **17**(7), 073005 (2015).
46. L. Medišauskas, U. Saalmann, and J. M. Rost, "Floquet hamiltonian approach for dynamics in short and intense laser pulses," J. Phys. B: At., Mol. Opt. Phys. **52**(1), 015602 (2019).
47. P.-L. He, Z.-H. Zhang, and F. He, "Young's Double-Slit Interference in a Hydrogen Atom," Phys. Rev. Lett. **124**(16), 163201 (2020).
48. W. C. Henneberger, "Perturbation method for atoms in intense light beams," Phys. Rev. Lett. **21**(12), 838–841 (1968).
49. M. Pont, N. R. Walet, and M. Gavrila, "Radiative distortion of the hydrogen atom in superintense, high-frequency fields of linear polarization," Phys. Rev. A **41**(1), 477–494 (1990).
50. K. L. Reid, "Photoelectron angular distributions," Annu. Rev. Phys. Chem. **54**(1), 397–424 (2003).
51. J. Itatani, J. Levesque, D. Zeidler, H. Niikura, H. Pépin, J. C. Kieffer, P. B. Corkum, and D. M. Villeneuve, "Tomographic imaging of molecular orbitals," Nature **432**(7019), 867–871 (2004).
52. M. Førre and A. S. Simonsen, "Nondipole ionization dynamics in atoms induced by intense xuv laser fields," Phys. Rev. A **90**(5), 053411 (2014).
53. T. E. Moe and M. Førre, "Ionization of atomic hydrogen by an intense x-ray laser pulse: An ab initio study of the breakdown of the dipole approximation," Phys. Rev. A **97**(1), 013415 (2018).